University of Groningen

Structure and kinematics of edge-on galaxy discs - II. Observations of the neutral hydrogen

Kregel, M.; van der Kruit, P. C.; de Blok, W. J. G.

IMPORTANT NOTE: You are advised to consult the publisher's version (publisher's PDF) if you wish to cite from it. Please check the document version below.

Document Version
Publisher's PDF, also known as Version of record

Link to publication in University of Groningen/UMCG research database

Structure and kinematics of edge-on galaxy discs – II. Observations of the neutral hydrogen

M. Kregel,[1] P. C. van der Kruit[1]* and W. J. G. de Blok[2]†

[1]*Kapteyn Astronomical Institute, University of Groningen, PO Box 800, 9700AV Groningen, the Netherlands*
[2]*Australia Telescope National Facility, PO Box 76, Epping NSW 1710, Australia*

ABSTRACT

We present Australia Telescope Compact Array and Westerbork Synthesis Radio Telescope H I observations of 15 edge-on spiral galaxies of intermediate to late morphological type. The global properties and the distribution and kinematics of the H I gas are analysed and discussed. We determine the rotation curves using the envelope-tracing method. For 10 spiral galaxies with a stellar disc truncation we find an average ratio of the H I radius to the truncation radius of the stellar disc of $1.1 \pm 0.2 \, (1\sigma)$.

Key words: galaxies: fundamental parameters – galaxies: kinematics and dynamics – galaxies: spiral – galaxies: structure.

1 INTRODUCTION

The neutral atomic hydrogen gas (H I) in spiral galaxies is highly dissipated, its bulk being confined to nearly circular orbits and forming a thin layer in the galaxy plane. This physical property makes the H I 21-cm emission line an excellent tracer of the circular velocity curves of spiral galaxies, and hence of their underlying radial mass distributions (e.g. Bosma 1978; Begeman 1987; de Blok, McGaugh & van der Hulst 1996). This also applies to the H I in spirals that are viewed edge-on, albeit that the velocity profiles are more complex due to the line-of-sight projection (Sancisi & Allen 1979; Sofue 1996; García-Ruiz, Sancisi & Kuijken 2002). Although challenging, the line-of-sight projection in edge-on spirals is actually much less complicated for the H I layer than for the old stellar disc (Kregel, van der Kruit & Freeman 2004a, hereafter Paper I). From a practical viewpoint, the signal-to-noise (S/N) ratio of H I synthesis observations is generally larger such that the H I can be studied at a higher velocity resolution. From the physical side, the H I velocity dispersion is typically 6–13 km s^{-1} (van der Kruit & Shostak 1982; Kamphuis 1993), much smaller than that of the old stellar population. Hence, the H I line-of-sight velocity profiles are mainly shaped by the density distribution and the rotation curve with only a small contribution from the H I velocity dispersion. The H I rotation curves of edge-on spirals may therefore be retrieved from the extreme-velocity envelope of the major axis position–velocity (XV) diagram (Sancisi & Allen 1979).

This is the second paper in a series[1] in which we aim to provide new constraints on the dynamics of spiral galaxy discs through

an observational synthesis of the global stellar disc structure and kinematics. The series is preceded by a re-analysis (Kregel, van der Kruit & de Grijs 2002, hereafter referred to as KKG) of the surface photometry in the *I*-band of the sample of edge-on galaxies from de Grijs (1997, 1998). In Paper I we presented optical spectroscopy to study the stellar kinematics in 17 edge-on galaxies taken from this sample. Here we present H I synthesis observations of 15 of the galaxies in the KKG sample and derive rotation curves using the envelope-tracing method. In Paper III we will introduce an automated method to derive rotation curves by fitting the full position–velocity diagrams. Also we will in Paper III further analyse the optical emission line spectroscopy (Paper I). From these combined H I and optical emission-line data we will determine the circular velocity curves and investigate the effects of absorption on our stellar kinematical data. In Paper IV (Kregel & van der Kruit 2004) we will model the stellar kinematics data of Paper I using the circular velocity curves and the stellar disc structure and finally present a general discussion in Paper V (Kregel, van der Kruit & Freeman 2004b).

Previously, H I synthesis observations were made only for three galaxies in our sample: NGC 891 (Sancisi & Allen 1979; Rupen 1991; Swaters, Sancisi & van der Hulst 1997), NGC 5170 (Bottema, van der Kruit & Freeman 1987) and NGC 5529 (Rhee & van Albada 1996). Here, we present both new 21-cm synthesis radio observations for 14 galaxies, including more sensitive observations of NGC 5170 and NGC 5529, and archival observations for four additional galaxies. The prime purpose of these H I observations is to provide detailed rotation curves for further use in later papers in the series. In addition, the morphology of the H I can be used to gauge environmental influences through the presence of tell-tale signs such as warping of the H I layer and the presence of companions.

The outline of this paper is as follows. In Section 2 the H I synthesis observations are presented and the reduction steps are summarized. The continuum and H I emission is analysed in Section 3.

*E-mail: vdkruit@astro.rug.nl
†Now at: Department of Physics and Astronomy, Cardiff University, 5 The Parade, Cardiff CF24 3YB.
[1] The series contains adapted versions of most chapters in the PhD thesis of MK (Kregel 2003).

This section also contains a brief investigation of the envelope-tracing method for determining the H I rotation curves. In Section 4 we explore the global H I properties of this sample of edge-on spirals. Finally, a summary is presented in Section 5. Throughout this series distances are calculated using the Virgo-centric velocities from the Lyon/Meudon Extragalactic Data base (LEDA, see table 1 in KKG) and a Hubble constant $H_0 = 75$ km s^{-1} Mpc^{-1}.

2 OBSERVATIONS AND DATA REDUCTION

2.1 New observations

The main observational parameters of both the new and the archival observations (Section 2.2) are given in Table 1. Among the 14 newly targeted galaxies, we decided to re-observe NGC 5170 and NGC 5529, because earlier observations lacked the sensitivity to determine their rotation curves with sufficient accuracy. The new 21-cm line observations were carried out during 2000–2001 using the Australia Telescope Compact Array (ATCA) and the Westerbork Synthesis Radio Telescope (WSRT). The new ATCA observations were performed with the array in one of its 1.5 km configurations (Table 1) and using the correlator configured to cover a bandwidth of 8 MHz with 1024 channels (1.6 km s^{-1} channel^{-1}). On-line Hanning velocity smoothing was not applied. To calibrate the flux density scale and the bandpass the source PKS B1934-638 was observed for 15 min at either the start or the end of each full synthesis observation. To allow proper correction of gain and phase changes the galaxy observations were interspersed every hour with a 5-min observation of a secondary calibrator.

Note that for three of the galaxies (ESO 263-G15, ESO 321-G10 and ESO 435-G50) the quality of the recorded optical spectra (Paper I) proved too low to determine their stellar kinematics. Their H I content does still contain valuable information and is included here.

The WSRT observations of NGC 5529 were carried out using the 'maxi–short' configuration. This configuration yields 52 baselines, the shortest being 36, 54, 72 and 90 m. The correlator provided 128 channels over a 10-MHz bandwidth (16.6 km s^{-1} channel^{-1}). On-line velocity tapering was not applied. Initial calibration was performed using the sources 3C 147 and CTD 93, after which a self-calibration procedure on the continuum map of the field surrounding NGC 5529 was used to perfect the calibration.

2.2 Archival observations

Four out of the six remaining galaxies in the sample of Paper I (ESO 240-G11, ESO 435-G25, ESO 437-G62 and ESO 487-G02) had been observed at 21 cm by Bureau, Freeman & Bosma with the ATCA (project no C529). These data were retrieved from the ATCA archive and will be investigated here. The archival ATCA observations were carried out in 6A, 6B and 1.5D array configurations and used 512 channels covering a 8-MHz bandwidth (3.2 km s^{-1} channel^{-1}). On-line Hanning velocity smoothing was not applied. These observations used the same calibration method as our new ATCA observations (Section 2.1). Details of the observations can be found in Table 1. Note that at 21 cm the primary beam sizes of the ATCA and WSRT are 33 and 36 arcmin at full width half maximum (FWHM), respectively. Hence, all targeted galaxies are well within the primary beam.

The two remaining galaxies, ESO 288-G25 and NGC 891, are not included here. The H I distribution of NGC 891 has been analysed in detail in previous studies (Sancisi & Allen 1979; Rupen 1991; Swaters et al. 1997). The H I rotation curve of NGC 891 will be re-analysed in Paper III, using the H I data of Swaters et al. (1997). For ESO 288-G25 H I synthesis observations are still lacking. Fortunately, the Hα major axis position–velocity diagram is well defined allowing an adequate determination of the rotation curve (Paper III).

2.3 The data reduction

The reduction of the visibility data was performed with the MIRIAD package. Using standard techniques, the visibilities were examined, interactively flagged for interference, and calibrated. A preliminary low spatial resolution data cube was then produced to locate the 21-cm line signal. The continuum signal was determined in the visibility domain by fitting a low-order polynomial to the line free channels, and subtracted. Spectral line data cubes and continuum maps were then created at three different spatial resolutions. A full resolution version was produced using robust weighting of the visibility data without further tapering (using robust values of 0.5 for the ATCA and 0.1 for the WSRT observations). Two lower resolution versions were obtained by applying a Gaussian taper to the visibility data with FWHM corresponding to 30 and 60 arcsec in the image domain. For the archival ATCA data, which included the 6-km array configuration, the low-resolution line cubes were created by applying a Gaussian taper with FWHM corresponding to 10 and 30 arcsec. Pixel sizes were chosen to be close to one-third of the synthesized beamwidth and the field was imaged out to the primary beam half power points. The velocity axis of the H I data cubes is heliocentric and uses the *radio* definition, yielding a constant velocity increment between channels. As a compromise between sensitivity and velocity resolution the ATCA data were averaged in velocity to yield 256 independent channels and a channel spacing of 6.6 km s^{-1}. The WSRT data of NGC 5529 were Hanning smoothed to suppress Gibbs ringing, yielding a velocity resolution of 33 km s^{-1} (FWHM).

Unfortunately, at this point it became clear that for three galaxies the sensitivity was insufficient: ESO 437-G62 remained undetected, whereas ESO 487-G02 and ESO 509-G19 were detected only after excessive velocity smoothing. The data for these galaxies were not further processed. The faintness of these sources is consistent with the single-dish flux densities derived using the HIPASS archive (Barnes et al. 2001).

The spectral line data cubes and continuum maps for the 15 detected galaxies were further processed and analysed within the GIPSY environment. First, the CLEAN algorithm was applied to correct for the effects introduced by limited visibility sampling. In each channel map, the region of H I emission to be *clean*ed was defined by a masked version of the 60-arcsec data cube. Following standard practice, this masked cube was created by retaining the H I emission in the channel maps above a level of twice the rms noise (2σ), and manually removing remaining noise peaks and grating rings. For the archival ATCA data the 30-arcsec resolution data cube was used to create these *clean* masks. Then, at each resolution, the areas defined by the masks were *clean*ed down to 0.5σ. The *clean* components were finally restored using a Gaussian beam with a FWHM similar to that of the central peak of the dirty beam. The continuum maps were *clean*ed using the same approach.

3 ANALYSIS

3.1 Radio continuum emission

21-cm continuum emission was detected in only five galaxies. Table 2 gives the continuum flux in the *clean*ed radio continuum maps at full resolution. The continuum fluxes are in agreement with

Table 1. Observing log.

Galaxy	Date	Time (hrs)	R.A.(J2000) (^{h} ^{m} ^{s})	Dec.(J2000) (^{d} ^{m} ^{s})	$v_{central}$ (km s^{-1})	Array	Beam (arcsec)	Noise (mJy beam^{-1})	(10^{19} cm^{-2})	Completeness (10^8 M$_\odot$)
(1)	(2)	(3)	(4)		(5)	(6)	(7)	(8)		(9)
ESO 142-G24	2000 Jan 8	12	19 35 42.3	−57 31 02	1998	1.5A	25.6 × 29.3	2.5	2.5	0.8
ESO 157-G18	2000 Nov 18	12	04 17 54.0	−55 55 47	1358	1.5E	22.1 × 29.5	3.2	3.6	0.4
ESO 201-G22	2000 Jan 1	12	04 08 59.3	−48 43 42	4153	1.5A	25.8 × 33.4	2.5	2.1	3.8
ESO 240-G11*	1996 Sep 16	12	23 37 49.4	−47 44 05	2856	6B	7.1 × 9.3	1.2	13	0.9
	1997 Mar 3	12	–	–	–	6A				
	1997 Mar 8	12	–	–	–	1.5D				
ESO 263-G15	2001 Mar 15	12	10 12 20.0	−47 17 39	2641	1.5D	25.5 × 30.1	2.6	2.5	1.4
ESO 269-G15	2001 Mar 10	12	12 57 13.0	−46 22 36	3503	1.5D	25.1 × 33.2	2.6	2.4	2.8
ESO 321-G10	2001 Mar 12	12	12 11 42.0	−38 32 53	3072	1.5D	26.1 × 36.9	2.6	2.0	2.4
ESO 416-G25	2000 Nov 15	12	02 47 60.0	−31 31 60	5023	1.5E	27.8 × 54.4	2.9	1.5	7.1
ESO 435-G14	2001 Mar 14, 16	8	09 57 48.0	−28 30 21	2641	1.5D	22.5 × 44.9	3.6	2.7	2.4
ESO 435-G25*	1996 Apr 6	12	09 59 55.7	−29 36 26	2427	6A	6.6 × 14.1	1.1	8.7	0.6
	1996 Sep 13	12	–	–	–	6B				
	1997 Mar 7	12	–	–	–	1.5D				
ESO 435-G50	2001 Mar 16	8	10 10 50.0	−30 25 25	2641	1.5D	22.7 × 41.5	3.5	2.8	2.4
ESO 437-G62*	1996 Apr 8	12	10 48 04.0	−31 32 28	2856	6A	8.1 × 14.9	1.8	11	1.5
ESO 446-G18	2001 Mar 11	12	14 08 38.0	−29 34 20	4805	1.5D	22.5 × 39.4	3.0	2.6	6.9
ESO 487-G02*	1996 Sep 15	12	05 21 48.7	−23 48 15	1785	6B	8.5 × 19.5	2.0	8.7	0.5
ESO 509-G19	2001 Mar 9	12	13 27 56.0	−25 51 24	11030	1.5D	25.2 × 53.5	2.6	1.5	30.3
ESO 564-G27	2000 Jan 9	12	09 11 54.7	−20 07 02	2212	1.5A	24.3 × 71.3	2.5	1.1	1.1
NGC 5170	2001 Mar 8	12	13 29 49.0	−17 57 57	1571	1.5D	23.7 × 73.0	3.1	1.3	0.7
NGC 5529	2001 May 16	12	14 15 34.3	+36 13 32	2920	Maxi-short	15.0 × 26.0	0.24	1.1	0.2

Columns: (1) name, an asterisk indicates archival data; (2) observing date; (3) observing time; (4) pointing centre; (5) central velocity of the bandpass; (6) array configuration; (7) full resolution synthesized beam; (8) root-mean-squared (rms) noise in the full resolution channel maps; (9) H i mass corresponding to a 5σ point source at the adopted galaxy distance having a velocity width of 50 km s^{-1}.

Table 2. Radio continuum fluxes.

| Galaxy | $S_{1.42\,GHz}$ | $\pm$ | $\log_{10} P_{1.42\,GHz}$ | $\pm$ |
| | (mJy) | | (W Hz^{-1}) | |
(1)	(2)	(3)	(4)	(5)
ESO 263-G15	17.0	1.4	21.28	0.04
ESO 435-G25	4.5	0.8	20.70	0.08
ESO 564-G27	3.7	1.3	20.51	0.16
NGC 5170	14.1	2.6	20.81	0.08
NGC 5529	22.4	0.9	21.66	0.02

Columns: (1) name; (2) and (3) continuum flux and error; (4) and (5) logarithm of the total power and error.

those found for galaxies of similar Hubble type (Hummel 1981). For ESO 435-G50 there is a very bright continuum source projected on to the receding side of the optical disc ($S_{1.42\,GHz} = 109$ mJy, not listed in Table 2). Interestingly, this bright source is double-lobed with the lobes apparently sticking out of the galaxy plane up to a projected height of ~30 arcsec (15 stellar disc scaleheights).

3.2 The neutral hydrogen emission

3.2.1 Global properties

The global profiles were constructed from the H I fluxes in the full resolution channel maps. In each of these channel maps the flux was calculated from the emission in the region of the *clean* masks and corrected for primary beam attenuation. The flux error was estimated by projecting the *clean* mask at eight different line-free locations, and integrating over each area separately. The standard deviation in the line-free 'fluxes' of these regions was then adopted as the flux error. For the four spirals for which companion satellites were also detected (see Section 3.4) only the emission from the main galaxy was included in the global profile. The resulting global H I profiles are presented in Fig. 2 (see below). The integrated primary beam corrected flux densities are listed in Table 3. The corresponding H I masses were calculated using the standard

formula: $M_{H_I} = 2.36 \times 10^5\, D^2 \int S\,dv$, where D is the distance of the galaxy in Mpc and $\int S\,dv$ is the flux density in Jy km s^{-1}. The basic assumption of this formula is that the H I is optically thin. This assumption clearly holds with respect to the continuum absorption, since for each galaxy the continuum flux is small compared with the line flux in a single channel. The effect of H I self-absorption is also small, according to a conservative estimate of the optical depth (see Paper III). The errors listed for the flux density and H I mass are the probable errors, calculated from the errors on the fluxes in the individual channels. The difference between the measured flux densities and those listed in LEDA (from single dish measurements) is shown in Fig. 1(a). The agreement is excellent, except for ESO 240-G11 and ESO 435-G25. For those the radio synthesis measurements yield lower flux densities. This missing flux is not surprising given that the angular sizes of ESO 240-G11 and ESO 435-G25 are significantly larger than the angular size corresponding to the shortest spacing used in the observations (~6 arcmin). There are no obvious confusing galaxies nearby on the sky. Note that considering the uncertainties the flux densities agree remarkably well for the remaining galaxies: the uncertainties in the LEDA fluxes are probably overestimated.

The H I global profiles were also used to calculate the systemic velocity and the linewidths at the 20 and 50 per cent levels. When double horned, the peak fluxes on the approaching and receding sides were used separately to determine these levels. Otherwise, the overall peak flux was used on both sides (which only applies to ESO 157-G18). The observed linewidths are listed in Table A1. The systemic velocity, listed in Table 3, was taken to be the average of the mid-points between the extreme velocities determined at 20 and 50 per cent of the peaks. The quoted velocities and linewidths use the optical velocity definition. The derived systemic velocities agree well with the LEDA values (Fig. 1b), although, as for the flux densities, the uncertainties quoted in LEDA have been overestimated. The observed linewidths were corrected for instrumental broadening and random motions according to the formalism of Verheijen & Sancisi (2001). Their instrumental correction is as follows:

Table 3. H I global properties.

| Galaxy | $\int S\,dv$ | $\pm$ | M_{H_I} | $\pm$ | v_{sys}† | $\pm$ | $W_{R,20}$† | $\pm$ | $W_{R,50}$† | $\pm$ | $R_{H_I}^{rece}$ | $R_{H_I}^{appr}$ |
| | (Jy km s^{-1}) | | (10^9 M$_\odot$) | | (km s^{-1}) | | (km s^{-1}) | | (km s^{-1}) | | (arcsec) | (arcsec) |
(1)	(2)	(3)	(4)	(5)	(6)	(7)	(8)	(9)	(10)	(11)	(12)	(13)
ESO 142-G24	22.9	0.3	2.9	0.1	1925.4	0.7	242.0	1.7	243.5	2.4	145	147
ESO 157-G18	16.3	0.3	0.8	0.1	1378.8	0.6	185.7	1.7	187.5	0.5	126	107
ESO 201-G22	14.2	0.2	8.7	0.1	4067.8	0.4	334.8	1.1	339.5	1.2	127	103
ESO 240-G11	49.7	0.5	14.7	0.2	2842.9	0.9	546.2	2.3	542.7	2.9	203	225
ESO 263-G15	19.5	0.4	4.3	0.1	2527.2	1.2	334.3	3.2	339.2	3.6	145	133
ESO 269-G15	8.6	0.2	3.7	0.1	3386.1	2.8	330.0	8.0	326.4	7.9	85	88
ESO 321-G10	3.9	0.2	1.4	0.1	3134.6	1.8	303.4	5.0	311.9	5.0	66	73
ESO 416-G25	9.7	0.2	9.5	0.2	4988.6	1.4	446.8	4.0	447.6	4.0	92	113
ESO 435-G14	16.0	0.4	4.1	0.1	2663.7	1.6	269.8	5.1	276.2	3.9	93	111
ESO 435-G25	44.1	0.3	9.7	0.2	2474.7	0.9	473.2	2.2	471.4	3.1	195	230
ESO 435-G50	7.3	0.3	2.0	0.1	2713.0	1.0	173.9	3.1	182.6	2.7	73	77
ESO 446-G18	8.2	0.3	7.4	0.3	4771.6	1.4	412.1	4.0	421.1	4.0	99	100
ESO 564-G27	39.7	0.4	6.8	0.1	2177.3	0.5	323.3	1.2	325.4	1.6	189	201
NGC 5170	91.1	0.6	8.2	0.1	1500.7	0.4	504.2	1.1	508.6	1.3	302	314
NGC 5529	43.2	0.3	17.4	0.1	2875.3	0.4	574.8	1.2	567.8	1.3	188	213

†The quoted velocities and linewidths use the optical velocity definition. Columns: (1) name (2) and (3) integrated flux density and error; (4) and (5) H I mass and error; (6) and (7) systemic velocity and error; (8) and (9) linewidth at the 20 per cent level and error; (10) and (11) linewidth at the 50 per cent level and error; (12) H I radius at the receding side; (13) H I radius at the approaching side.
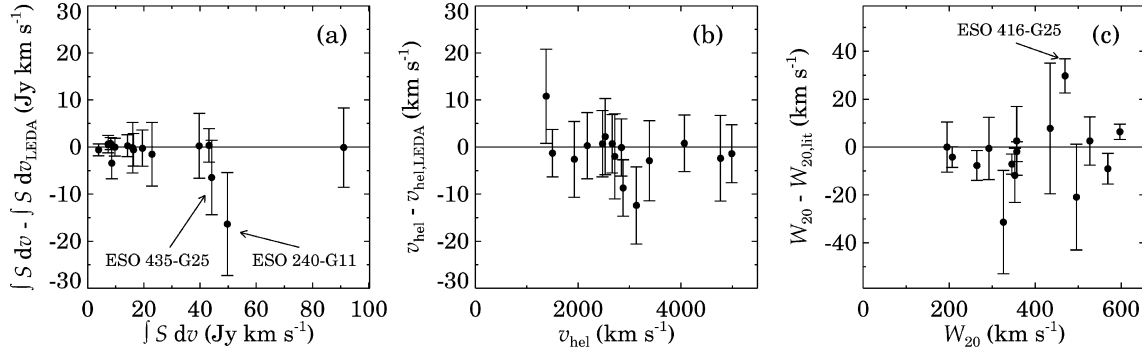
Figure 1. A comparison with the literature for (a) the flux densities, (b) systemic velocities and (c) linewidths at the 20 per cent level (see the text).

$$W_{20} = W_{20,obs} - 35.8 \left[\sqrt{1 + (R/23.5)^2} - 1 \right], \quad (1)$$

$$W_{50} = W_{50,obs} - 23.5 \left[\sqrt{1 + (R/23.5)^2} - 1 \right], \quad (2)$$

where R is the velocity resolution in km s^{-1} (FWHM). This correction is based on approximating the edges of the global profile, which are mostly due to turbulent motion, with a Gaussian dispersion of 10 km s^{-1}. The corrections typically amount to a 20–25 km s^{-1} reduction in width. To enable a meaningful comparison of the corrected widths with the literature, the raw literature values were gathered (Table A1) and corrected for instrumental broadening in the exact same way. The derived widths at the 20 per cent level are compared with these literature values in Fig. 1(c). The linewidths are in agreement; the weighted mean of the difference $W_{20} - W_{20,lit}$ is -0.4 ± 1.6 km s^{-1}, whereas the rms scatter is 14 km s^{-1}. For the linewidths at 50 per cent level the agreement is comparable (not shown).

The correction for random motion is based on the empirical formula of Tully & Fouque (1985):

$$W_{R,l}^2 = W_l^2 + W_{t,l}^2 \left[1 - 2\exp - \left(\frac{W_l}{W_{c,l}} \right)^2 \right]$$

$$- 2W_l W_{t,l} \left[1 - \exp - \left(\frac{W_l}{W_{c,l}} \right)^2 \right], \quad (3)$$

where the subscript l refers to the level at which the linewidth was determined, $W_{c,l}$ is the linewidth which defines the transition between quadrature summation (at small linewidths) and a linear correction (at larger linewidths), and $W_{t,l}$ is a constant representing the H I random motions. We adopt $W_{c,20} = 120$, $W_{c,50} = 100$ and $W_{t,20} = 22$, $W_{t,50} = 5$ km s^{-1} in order to probe the maximum rotation (Verheijen & Sancisi 2001). The corrected linewidths are listed in Table 3.

3.2.2 The H I distribution

The H I column density maps were obtained by taking the zeroth moment of the masked channel maps (Fig. 2). Since the area containing H I emission is different in each channel, the noise in the column density map varies according to the number of channels summed at each position. To facilitate the interpretation of the H I column density maps, this noise map was calculated according to $\sigma_{total} = (n_{chan})^{1/2} \sigma$, where n_{chan} is the number of summed channels and σ is the actual rms noise level in a single channel map (the correlated

noise introduced by the continuum subtraction is negligible). For NGC 5529 the data were Hanning smoothed. In this case we used $\sigma_{total} = (n_{chan} - \frac{3}{4})^{1/2} \frac{4}{\sqrt{6}} \sigma$ (Verheijen & Sancisi 2001). From the column density map and this noise map a signal-to-noise ratio map was constructed. Then, the average flux density of the pixels in the column density map with a signal-to-noise ratio between $2\frac{3}{4}$ and $3\frac{1}{4}$ was calculated. This signal-to-noise ratio level is indicated in Fig. 2 by a thick contour.

The line-of-sight projection of an edge-on H I layer entails that each observed position contains information on a large range of galactocentric radii. The face-on H I surface density profile can be retrieved by deprojecting the observed radial H I distribution under the usual assumptions that the H I distribution is optically thin and axisymmetric. Any large deviations from axisymmetry can then be investigated by comparing the results from the approaching and the receding sides. The observed radial H I distribution was deprojected following the method outlined in Warmels (1988). First, the so-called strip integral was calculated by integrating the H I column density map perpendicularly to the major axis, as defined by the dynamical centre and position angle of the stellar disc (table 4 in Paper I). The approaching and the receding sides of this strip integral are deprojected separately, using Lucy's (1974) iterative deconvolution method. The iteration process is halted at the point at which it produces a reduction in χ^2 less than 10 per cent (typically at 10–15 iterations). The inferred face-on H I surface density profiles are plotted in Fig. 2. The radii at which the azimuthally averaged H I surface density drops below 1 M$_\odot$ pc^{-2} were determined for the approaching and the receding side separately. These H I radii are listed in Table 3.

Note that Warmels' (1988) method has two disadvantages. First, it overestimates the H I surface density in the central parts (at radii smaller than 1–2 beam FWHM, Warmels 1988; Swaters 1999). For a poorly resolved edge-on spiral this may lead to an overinterpretation of the major axis position–velocity diagram: rotational velocities could be assigned at small radii even when in reality no H I is present. Secondly, although comparing the receding and approaching sides gives a rough estimate, the method does not provide error estimates. These effects are important for most of our galaxies. In Paper III, an alternative method will be introduced, which attempts to lift these drawbacks by determining both the H I surface density profile and the rotation curve from the position–velocity diagram.

Finally, the H I column density map was also used to determine the projected H I layer thickness as a function of projected radius. For this, Gaussians were fitted to profiles extracted from a H I column density map that was constructed from a version of the channel maps smoothed to a circular beam. These profiles were extracted perpendicularly to the major axis at an interval corresponding to
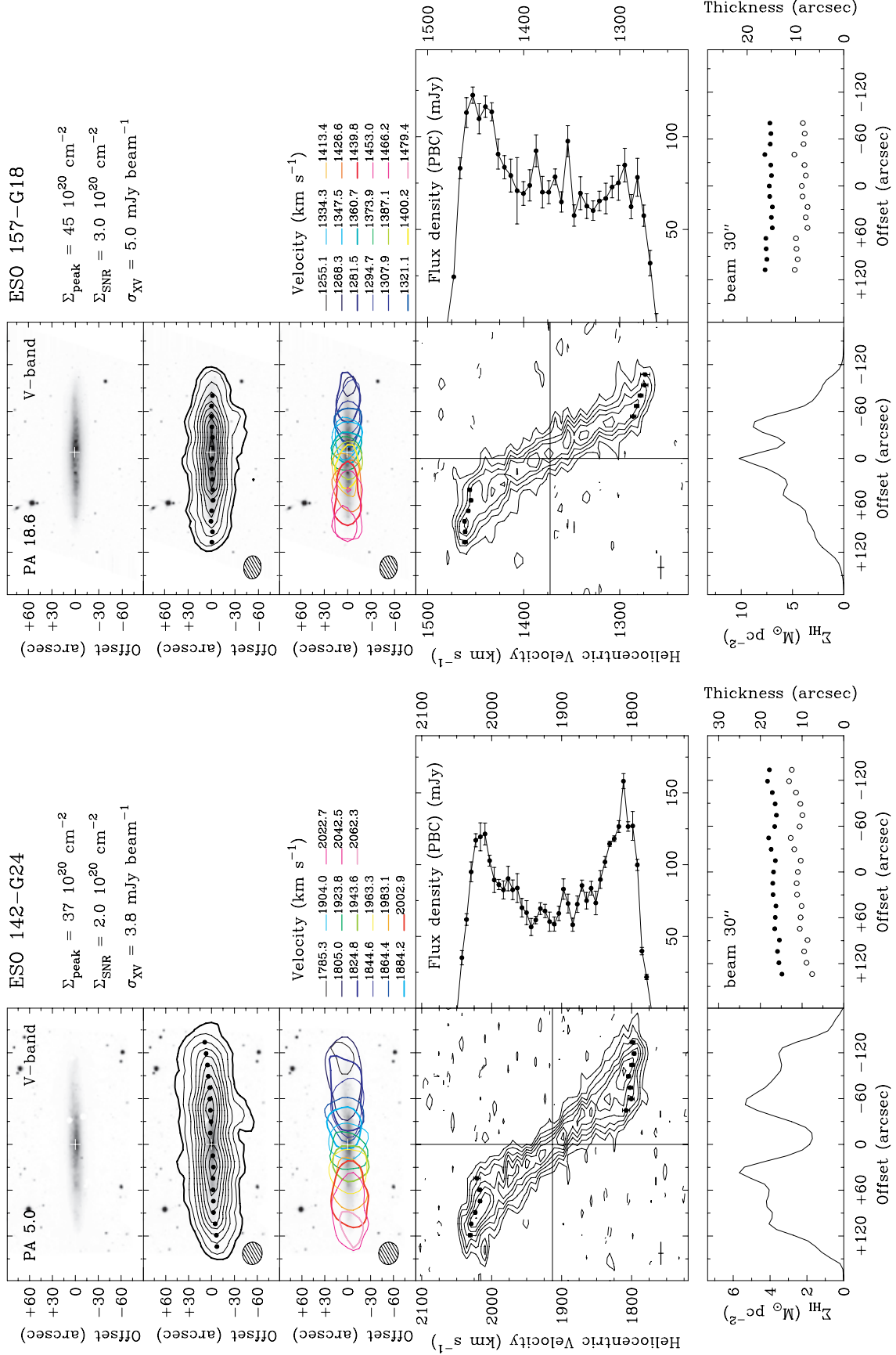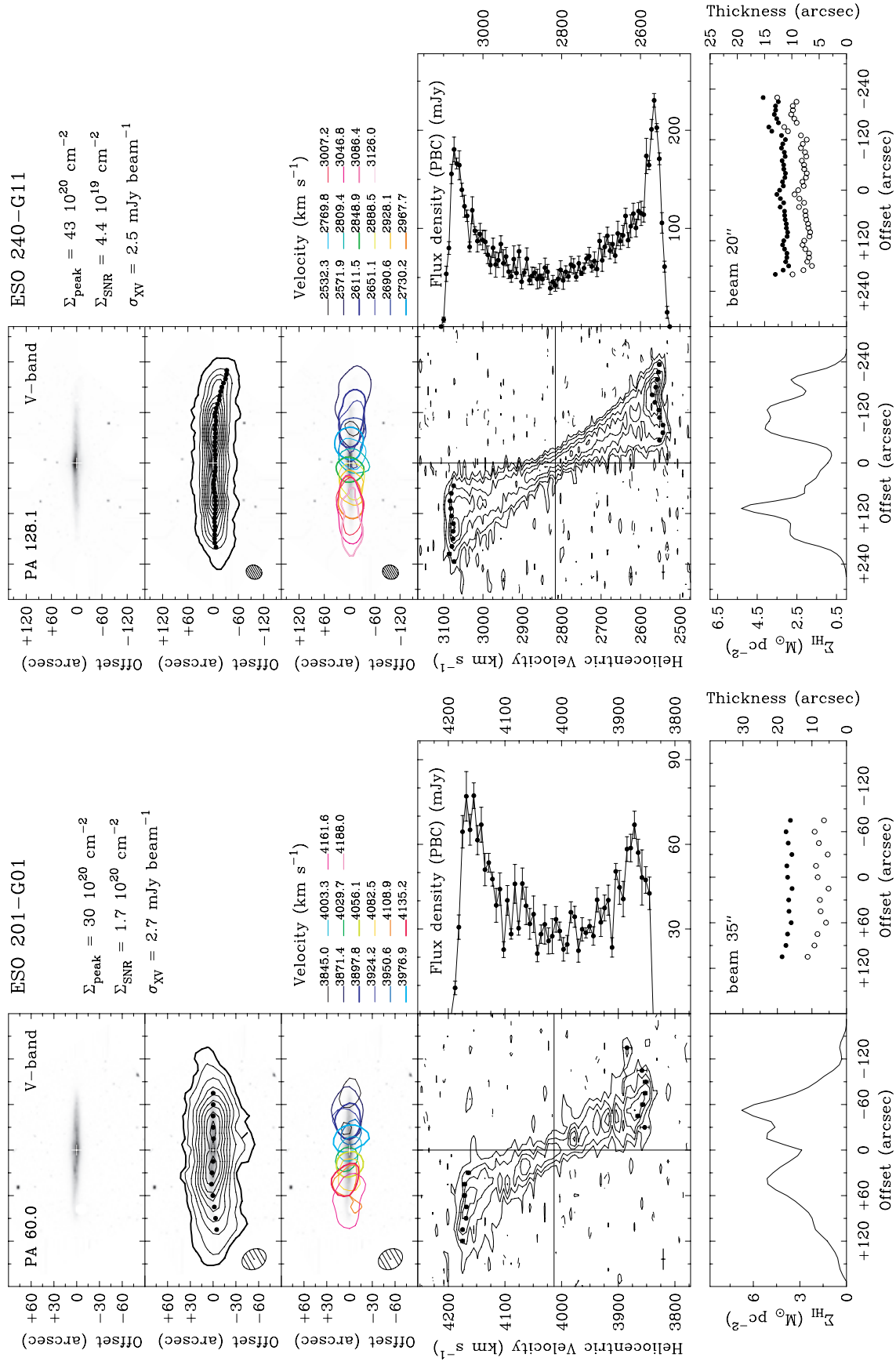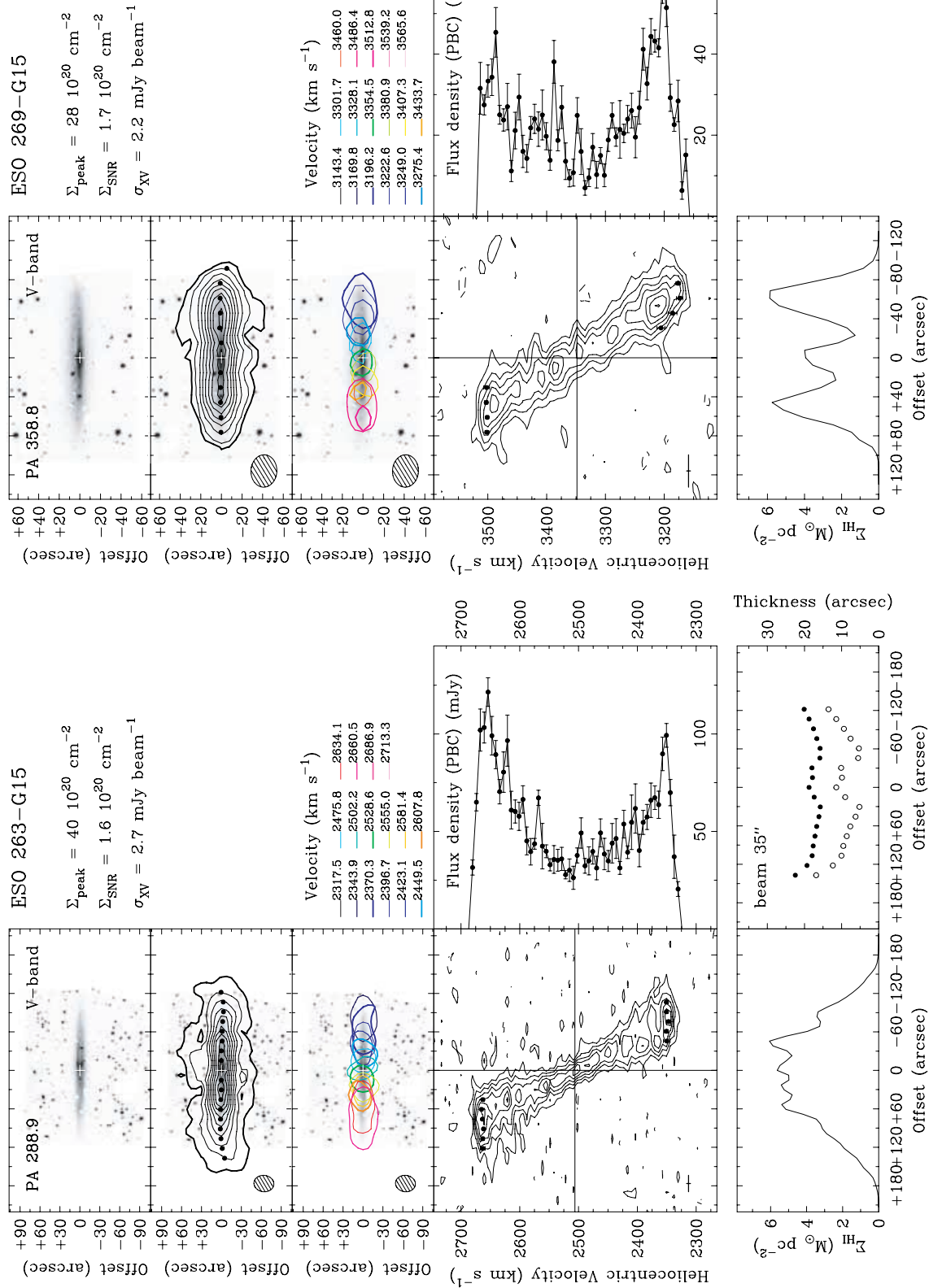
Figure 2. The H I distribution and kinematics for the full sample. A detailed description is given in Section 3.2.5.
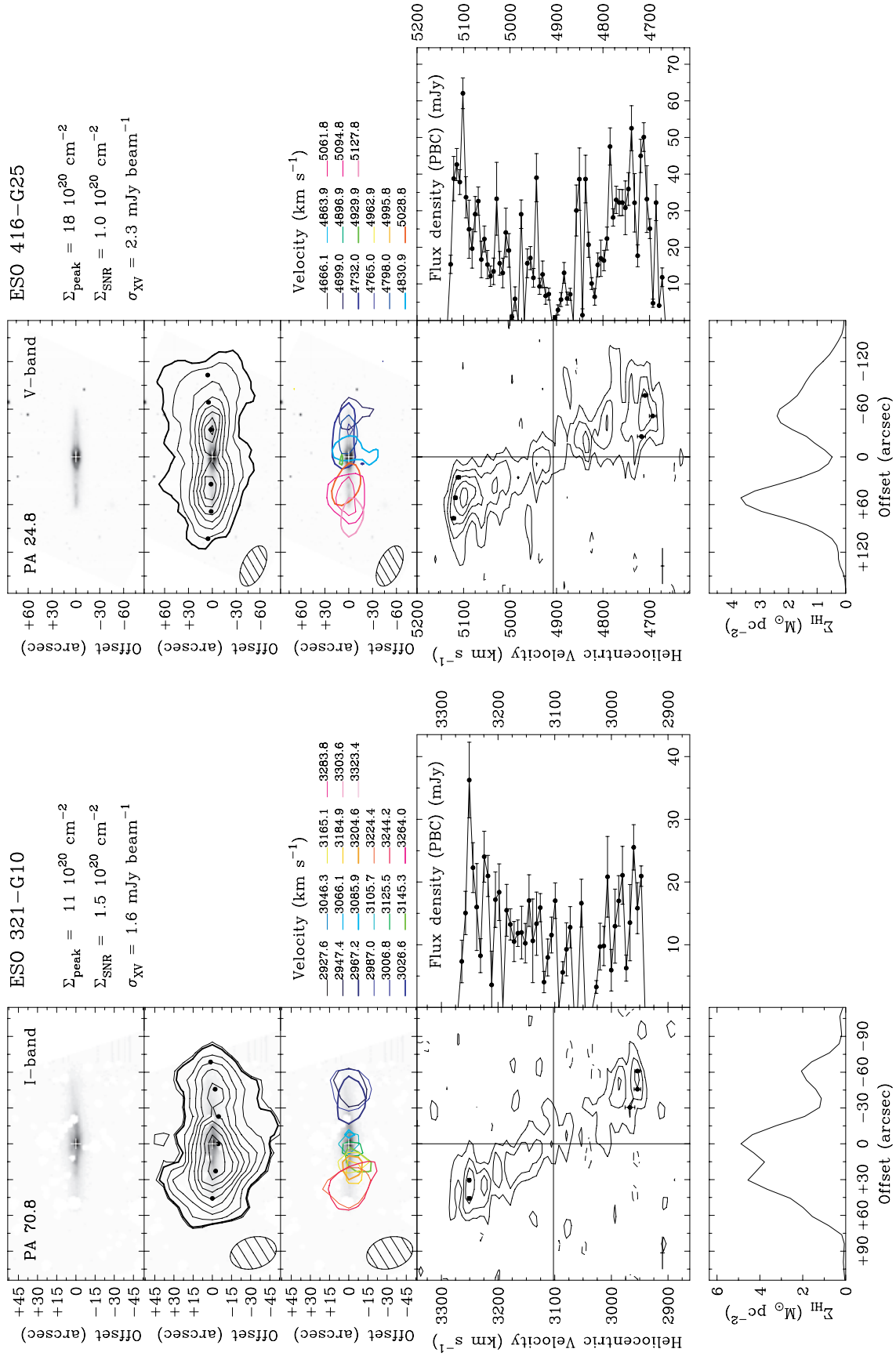
Figure 2 – *continued* – ESO 240–G11. The H I column density map, renzogram and XV diagram were taken from the 30-arcsec resolution data cube (synthesized beam 32.6 × 38.4 arcsec²). The XV diagram contour levels are −4, −2, 2, 4, 8, 12, 16, 20 and 24 times σ_{XV}.
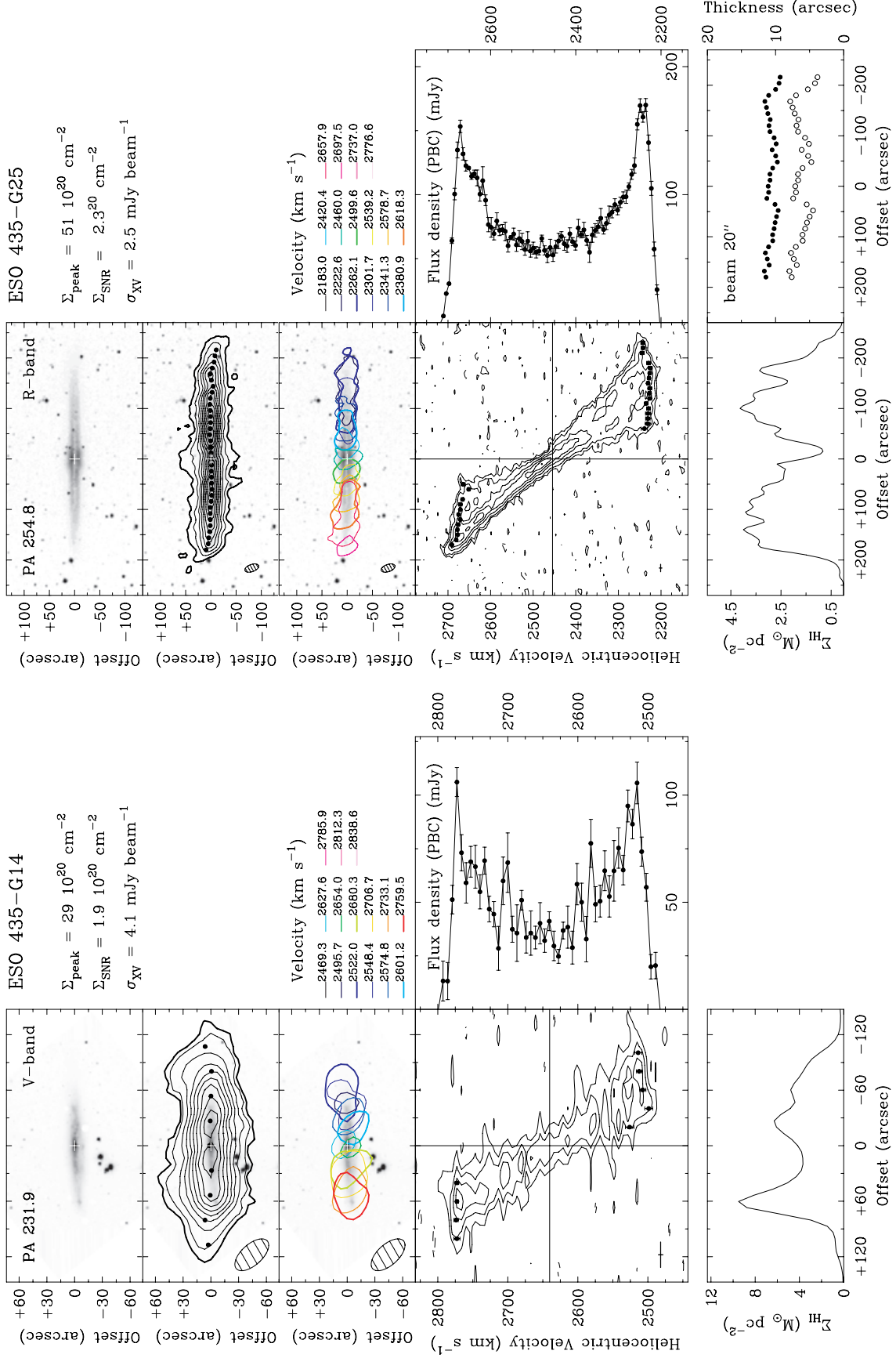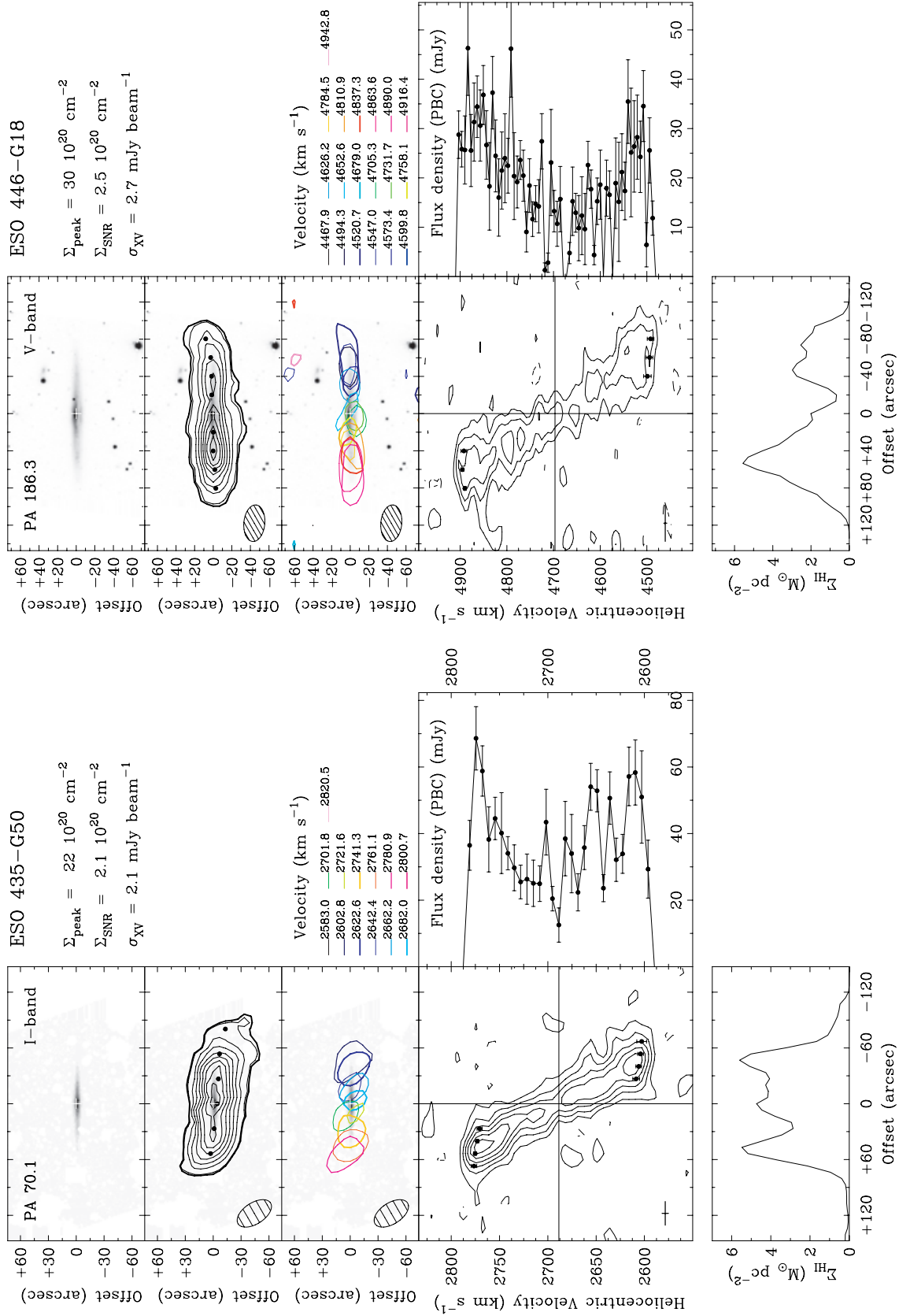
Figure 2 – *continued* – ESO 269-G15. The XV diagram has been Hanning smoothed.

Figure 2 – *continued* – ESO 321-G10. The renzogram was constructed using the Hanning-smoothed data cube and a level of 3σ. ESO 416-G25. The renzogram was constructed using a level of 3σ. Both XV diagrams were Hanning smoothed.

Figure 2 – *continued* – ESO 435-G25. The H I column density map, renzogram and XV diagram were taken from the 10-arcsec resolution data cube (synthesized beam 14.3×28.8 arcsec^2). The XV diagram contour levels are -4, -2, 2, 4, 8, 12, 16, 20 and 24 times σ_{XV}.

Figure 2 – *continued* – ESO 435-G50. The XV diagram has been Hanning smoothed. The renzogram was constructed using a level of 3σ.
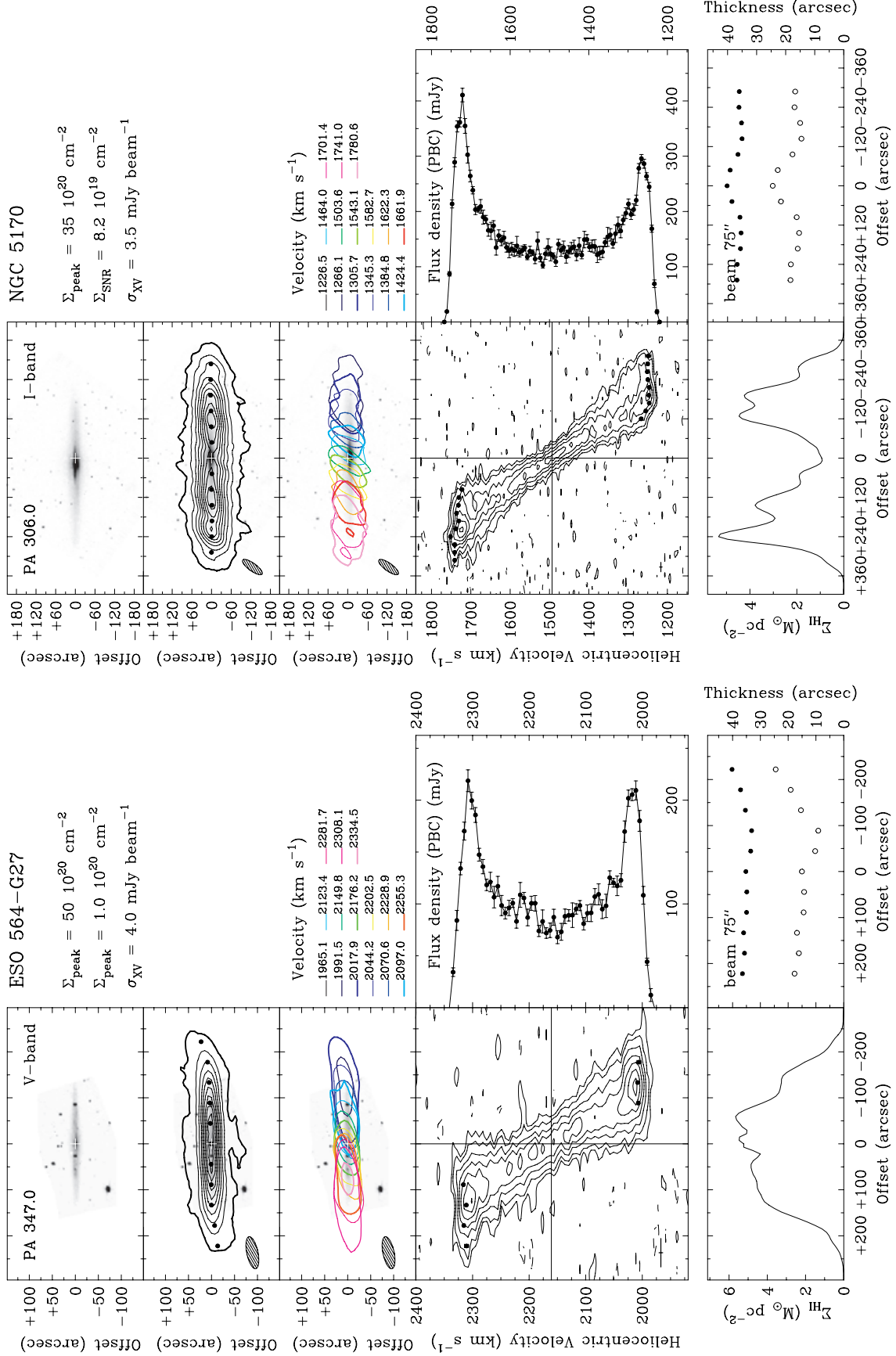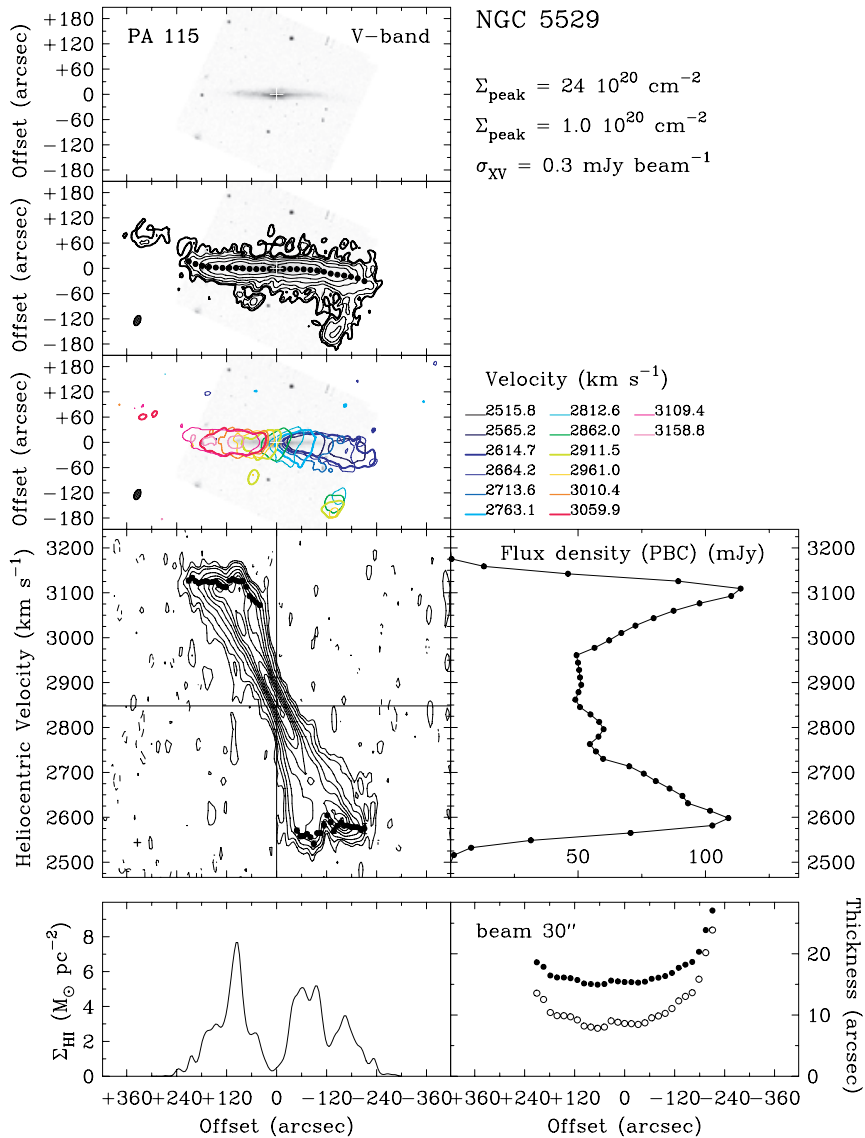
Figure 2 – *continued* – For ESO 564-G27 and NGC 5170 the contour levels in the XV diagram are −4, −2, 2, 4, 8, 12, 16, 20 and 24 times σ.

Figure 2 – *continued* – NGC 5529. Contour levels in the XV diagram are −4, −2, 2, 4, 8, 16, 24, 32, 40, 48 and 56 times σ. Contour levels in the H I column density map are 1.9, 3.8, 7.6, 15.2, 30.4 and 60.8 × 10^{20} cm^{-2}.

two-thirds of the circular beam FWHM. The fitted Gaussian centroids and 1σ dispersions are shown in Fig. 2 (after correction for instrumental broadening).

3.2.3 The H I kinematics

The H I kinematics were studied using the major axis position–velocity diagrams (see Fig. 2). These XV diagrams were extracted from the full resolution data cubes by integrating the H I emission perpendicularly to the major axis as defined by the stellar disc centre and position angle (table 4 in Paper I). For NGC 5529, which has two nearby satellites connected to the main galaxy via H I bridges (Section 3.3), the anomalous H I was excluded while forming the XV diagram.

In first instance, the H I rotation curves were derived from these XV diagrams using the envelope-tracing technique, also often referred to as the terminal-velocity or edge-fitting method (Sancisi & Allen 1979; Olling 1996; Sofue 1996; García-Ruiz et al. 2002). In Paper III we will discuss the drawbacks of this method and in-

troduce a new one that takes account of the effects of the line-of-sight projection and beam smearing. The basic assumptions of the envelope-tracing method are that the H I is (i) in perfect circular rotation and (ii) detected everywhere along the line-of-nodes. Under these assumptions the extreme-velocity envelope of the major axis XV diagram traces the H I along the line of nodes. Provided that a proper correction is made for instrumental broadening and turbulent motion this envelope can thus be used to derive the rotation curve. This correction, in essence a deconvolution, is what differs between the various implementations of the envelope-tracing method in the literature.

Here, a series of Gaussian least-squares fits was made to the extreme-velocity side of each velocity profile along the major axis (see García-Ruiz et al. 2002 for an illustration). In these fits the Gaussian dispersion was fixed at $\sigma_G = (\sigma_{HI}^2 + \sigma_{instr}^2)^{1/2}$, where σ_{HI} is the H I velocity dispersion and σ_{instr} is the velocity resolution. According to H I observations of face-on galaxies the turbulent motion of the H I is characterized by a vertical velocity dispersion of approximately 8–13 km s^{-1} within the region of the stellar disc and

6–8 km s^{-1} at larger radii, (van der Kruit & Shostak 1982; Dickey, Hanson & Helou 1990; Kamphuis 1993). For our present purpose we are mainly interested in the region corresponding to the stellar disc and, assuming that the H I velocity dispersion is isotropic, we adopt a constant value $\sigma_{H_I} = 10$ km s^{-1}. In each Gaussian fit in the series, the upper fitting boundary was fixed at the highest velocity showing emission above three times the rms noise level. In the first fit, three channels towards lower velocities were included, in the second four channels, etc., until the channel corresponding to the peak emission was reached (cf. García-Ruiz et al. 2002). The fit with the smallest reduced χ^2 was retained as the best fit, with the peak velocity of the fitted Gaussian defining the rotation. The errors are estimated according to the formula of García-Ruiz et al. (2002) derived from Monte Carlo simulations: $\sigma_{v_c} = 4\sigma_G/\sqrt{n_{ps}}$ (S/N), where n_{ps} is the number of channels per σ_G and S/N ratio is the ratio of the amplitude of the fitted Gaussian to the rms noise level in a single channel.

The derived rotation curves are overlaid on the major axis XV diagrams in Fig. 2. While in general the least-squares fits to each of the major axis velocity profiles were well behaved, in first instance they did not converge for ESO 157-G18, ESO 435-G14 and ESO 446-G18. This was caused by the fact that the extreme-velocity side of the velocity profiles is steeper than that implied by an H I velocity dispersion $\sigma_{H_I} = 10$ km s^{-1}. For these galaxies σ_{H_I} was lowered until the fits did converge, yielding values of 6 km s^{-1} for ESO 157-G18 and ESO 446-G18, and 7 km s^{-1} for ESO 435-G14. Since ESO 157-G18 and ESO 435-G14 are small spirals, this would suggest that the H I velocity dispersions are smaller in dwarfs. However, ESO 446-G18 is clearly a massive spiral, and for the other two small systems in the sample (ESO 142-G24 and ESO 435-G50) the fits using $\sigma_{H_I} = 10$ km s^{-1} were well behaved.

3.2.4 Data presentation

The H I distribution and kinematics of each galaxy is presented in Fig. 2. From left to right and top to bottom, these figures show the following.

(i) Optical image. The first panel shows an optical image rotated according to the centre and position angle of the stellar disc (table 4 in Paper I). The white cross marks the dynamical centre. The position angle and the optical passband are indicated in the upper left and right, respectively.

(ii) Column density map. The H I column density distribution at full resolution (corrected for primary beam attenuation) overlaid on the optical image. Contour levels are $1/9, 2/9, \ldots, 8/9$ times the peak column density, unless the figure caption indicates otherwise. The thick contour corresponds to the signal-to-noise ratio level of three. The dots indicate the loci of the peaks of the Gaussians fitted to the vertical H I distribution. The peak column density and the average column density at the signal-to-noise ratio level of three are listed next to the plots.

(iii) Renzogram. The so-called renzogram, overlayed on the optical image, shows for a number of full resolution channel maps a contour drawn at four times the rms noise level. A renzogram is a compact way of showing the H I distribution in the channel maps. The contour line styles and the corresponding helio-centric velocities (radio definition) for each of the selected channels are listed next to this panel.

(iv) XV diagram. The integrated position–velocity diagram (radio definition). Contour levels are $-4, -2, 2, 4, 6, 8$, etc, in units of the rms noise in the XV diagram, unless indicated otherwise in

the figure caption. The rms noise (σ_{XV}) is listed next to the plots. The dots show the rotation curve derived using the envelope-tracing method. The horizontal and vertical lines denote the dynamical centre and the H I systemic velocity, respectively. The spatial and velocity resolutions (FWHM) are indicated by the cross in the lower left.

(v) Global profile. Primary beam corrected H I flux as a function of helio-centric velocity (radio definition).

(vi) Surface density profile. Face-on H I surface density profile obtained using the method of Warmels (1988).

(vii) Projected thickness. The dispersion obtained by fitting Gaussians to the (projected) vertical H I distribution as a function of projected radius, both before (dots) and after (circles) correction for the spatial resolution. The circular beam of the smoothed version of the H I column density map is indicated. This panel is omitted when the vertical distribution is unresolved.

3.3 Notes on individual galaxies

ESO 142-G24. The H I radius is only slightly larger than the stellar disc, which has a truncation at radius $R_{max} = 130$ arcsec (KKG). The H I appears to be warped on both sides, following a pattern similar to that of the stellar disc. The distinct H I feature detected in the XV diagram at a projected radius of 140 arcsec and 2020 km s^{-1} lies just outside our optical image. The tentative H I extension in the column density map (approaching side) is an artefact of the continuum subtraction.

ESO 157-G18. This dwarf system is lopsided, both in terms of its H I kinematics and density distribution. This is directly apparent from the global profile, which is single peaked, and the XV map, which reflects a slowly rising/flat rotation curve at the approaching/receding side. No H I is detected at radii beyond the stellar disc. The lopsidedness may be related to the presence of the small companion APMBGC 157 + 052 + 052 (Section 3.4), or the proximity of the S0 liner NGC 1553 and/or the elliptical NGC 1549.

ESO 201-G22. Radially, the H I is more extended at the receding side, causing an asymmetry in the global profile. At that side, the H I extends well beyond the stellar disc (stellar truncation radius $R_{max} = 102$ arcsec, KKG). On the approaching side H I emission is detected at the 4σ level outside the stellar disc ($R \simeq 130$ arcsec), having a velocity 20–30 km s^{-1} lower than the H I at smaller radii. The vertical H I distribution is barely resolved.

ESO 240-G11. Although the H I in this fairly massive spiral is not detected far beyond the stellar disc, it appears to show a mild thickening just beyond R_{max} (210 arcsec). On the approaching side the thickening is accompanied by a warping of the H I. XV diagrams taken parallel to and away from the major axis show that the warp forms a linear structure in the XV diagram, as if confined to a ring. Interestingly, the H I warp can be identified with faint emission in the *I*-band image. Further in, the H I is dominated by a ring or spiral arm with a radius ∼120 arcsec. At the receding side, the XV diagram is dominated by a curved structure, perhaps a strong spiral arm. The projected outer edge of this structure, at $R \simeq 90$ arcsec, coincides with a 'knee' in the *I*-band surface brightness distribution (cf. fig. A1 in KKG).

ESO 263-G15. The H I is more extended at the receding side, causing an asymmetry in the global profile. The XV diagram is regular and consistent with a flat rotation curve beyond 40 arcsec. The low level signal away from the galaxy plane is artificial.

ESO 269-G15. The density profile is fairly symmetric. The XV diagram on the other hand is asymmetric, the most striking being that the highest H I densities on the approaching side do not correspond to extreme-velocity envelope. On this side the H I appears to be in solid-body rotation, while on the receding side the rotation curve seems to reach a flat part. No H I was detected beyond the stellar disc.

ESO 321-G10. This small Sa is structurally lopsided in H I. The rotation curve is poorly resolved spatially. For the dynamical centre the optical centre was taken (table A1 in KKG).

ESO 416-G25. On the approaching side the H I is more extended, reaching well beyond the truncation radius (R_{max} = 74 arcsec). The peak face-on surface density on this side is almost twice as low as that on the receding side.

ESO 435-G14. Although the global profile is rather symmetric, the face-on surface density profiles are very different at both sides. The H I clearly extends further than the optical disc (R_{max} = 80 arcsec).

ESO 435-G25. The H I in this large Sc spiral, which has a peanut-shaped bulge, displays rich structure in its distribution and kinematics. First, the H I, like the stars, extends to larger projected radii on the approaching side. Secondly, there is a moderate warping of the H I on both sides. On the approaching side this warp is also observed in the optical. On that side the rotation curve is approximately flat until it shows a drop of approximately 20 km s^{-1} coinciding roughly with the onset of the warp ($R \sim 200$ arcsec). On the receding side the warping appears to be smaller. On this side the XV diagram is dominated by a curved high-density ridge. Inspection of the data cube at full resolution shows that this ridge is actually a superposition of multiple linear features (rings). The extreme-velocity envelope at the receding side is slowly rising from $R = 50$ up to 160 arcsec and shows a remarkable upturn in the outskirts, reaching velocities higher than on the approaching side. Finally, the data hint at a vertical extension in the central region. Deeper observations are needed to confirm this.

ESO 435-G50. The column density map shows a strongly warped H I distribution. The stellar disc does not appear to follow this H I warp. The rotation curve rises up to the last measured point.

ESO 446-G18. Most of the H I emission of this galaxy is located on the receding side. On the approaching side, the H I shows an upturn which in the optical image coincides with a structure that resembles a spiral arm. The peak in the face-on surface density profile from the receding side coincides roughly with the 'knee' present in the *I*-band surface brightness distribution (cf. fig. A1 in KKG).

ESO 564-G27. This Sc is rather symmetric, both in density and kinematics. The H I extends further than the stellar disc (R_{max} = 148 arcsec). In addition, it is warped on both sides, with the warp apparently starting outside the stellar disc. The rotation curve shows a local maximum on the receding side, at a projected radius of approximately two disc scalelengths.

NGC 5170. The H I is structurally lopsided. At the present sensitivity the H I does not extend far beyond the stellar disc. A local maximum is remarkable in the rotation curve on the receding side at $R \sim 240$ arcsec. This maximum corresponds to the projected end of a curved structure, probably a spiral arm, which dominates the XV diagram on that side. On the approaching side an inner ring-like structure with $R \sim 120$ arcsec dominates.

NGC 5529. This spiral is probably barred (Paper III, appendix). In addition, its H I layer is warped, and, like the stellar disc, strongly perturbed on the approaching side. Hence, it is likely that a substantial fraction of the H I follows non-circular orbits, at least in the inner parts ($R \lesssim 50$ arcsec). In that region, the extreme-velocity envelope is not representative of the circular velocity curve. On the approaching side, the envelope rises sharply and peaks at a velocity of approximately 290 km s^{-1} at $R \sim 90$ arcsec. Further out, at $R \sim 120$ arcsec it shows a steep drop with a minimum of 245 km s^{-1}, which is followed by a gradual increase. Two small companions are located south of and close to the perturbed H I layer at a velocity close to the systemic velocity of NGC 5529. Interestingly, these companions are connected to the main galaxy via low column density H I bridges (see also Section 3.4). On the receding side, the envelope is less steep but again shows a local minimum at $R \sim 120$ arcsec. The H I on the receding side is also warped. It further shows a faint extension to larger projected radii with an H I mass of approximately 3.1×10^8 M$_\odot$. This gas cannot be identified with an optical companion and may be part of the warped H I layer.

3.4 Companion galaxies

The H I data cubes were searched for the presence of companion galaxies. Table 1 gives for each of the data cubes an indication of the mass sensitivity. In four data cubes, those of ESO 157-G18, ESO 240-G11, ESO 435-G25 and NGC 5529, a total of seven companions are detected. Their main properties are listed in Table 4. Each of these is discussed in the following.

Table 4. Companion galaxies detected in H I.

Galaxy	Companion	R.A. (h m s)	Dec. (d m s)	Vel. range (km s^{-1})	M_{HI} (10^8 M$_\odot$)	$\int S \, dv$ (Jy km s^{-1})
(1)	(2)	(3)	(4)	(5)	(6)	(7)
ESO 157-G18	APMBGC 157+052+052	04 18 07.7	−55 55 43	1373–1420	0.2	0.5
ESO 240-G11	ESO 240-G13	23 39 26.9	−47 46 27	3131–3388	7.3	1.9
	APMBGC 240-032-114	23 36 24.4	−47 41 00	2742–2897	5.9	2.0
ESO 435-G25	A*	10 00 44.7	−29 31 12	2635–2715	13.0	5.9
	B*	10 01 00.9	−29 44 40	2247–2338	1.2	0.5
NGC 5529	MCG +06−31−085a	14 15 18.8	+36 12 08	2826–2990	6.7	1.7
	B*	14 15 35.5	+36 12 02	2928–2990	1.3	0.3

Columns: (1) main galaxy; (2) companion, an asterisk indicates the companion is listed neither in LEDA nor in the NASA/IPAC Extragalactic Data base; (3) and (4) companion central position; (5) companion velocity range (heliocentric, optical definition); (6) companion H I mass (using the adopted distance of the main galaxy); (7) companion integrated flux density.

ESO 157-G18. APMBGC 157+052+052 is located at a projected distance of 110 arcsec or approximately three disc scalelengths. Its apparent magnitude in *I*-band was determined using the photometry of de Grijs (1998) to be $m_I = 14.87$ mag. At the adopted distance of the main galaxy this translates to a luminosity $L_I = 1.2 10^8$ L$_\odot$ (using M$_{\odot,I} = 4.11$), or approximately 10 per cent of the *I*-band luminosity of ESO 157-G18. An interesting feature is an offset of ~ 7 arcsec (one-third of the FWHM of the synthesized beam) between the H I and the optical centres of this companion. It is conceivable that this offset has resulted from an ongoing interaction with ESO 157-G18.

ESO 240-G11. At a projected distance of approximately 17 arcmin or approximately 20 disc scalelengths we find the small SBb galaxy ESO 240-G13. It has an *I*-band magnitude $m_I = 12.41$ (Mathewson & Ford 1996) corresponding to a luminosity $L_I = 6.2 10^9$ L$_\odot$ (M$_{\odot,I} = 4.14$). Together with ESO 240-G11 and ESO 240-G10 (not detected), ESO 240-G13 forms an isolated triple system (Karachentseva & Karachentsev 2000). The second detection, APMBGC 240-032-114 is a small companion to ESO 240-G11 at a projected distance of 14 arcmin or 18 disc scalelengths. Its photographic magnitude $B_J = 15.87 \pm 0.12$ (Loveday 1996) corresponds to $L_B = 8.8 10^8$ L$_\odot$ (M$_{\odot,B} = 5.48$).

ESO 435-G25. The optical counterpart of companion A at a projected distance of 12 arcmin (12 disc scalelengths) has an irregular appearance on the Digital Sky Survey (DSS). Companion B, at 14 arcmin (14 disc scalelengths), has only one-tenth of the H I mass of companion A and is barely visible on the DSS. Given their small velocity differences with the systemic velocity of ESO 435-G25, both companions are probably satellites (both are outside the optical images of de Grijs 1998).

NGC 5529. MCG +06-31-085a is located at a projected distance of 3.5 arcmin (2.5 arcmin from the galaxy plane) and is connected to NGC 5529 via an H I bridge. The H I associated with this bridge amounts to approximately 6.5×10^8 M$_\odot$. Companion B is found at a projected distance of approximately 30 arcsec from the plane of NGC 5529 and also appears to be connected to NGC 5529 via a bridge.

4 DISCUSSION

Although the main purpose of the present H I observations is to determine the H I rotation curves, the global H I properties also provide valuable information.

4.1 The H I mass–luminosity relation

It has been well established that spirals of higher optical (or near-infrared) luminosity tend to have a larger H I mass (Roberts & Haynes 1994; de Blok et al. 1996; Broeils & Rhee 1997). This is illustrated in Fig. 3(a) for our sample of edge-on spirals, where we plot the H I mass versus the *I*-band absolute magnitude. For the ESO-LV galaxies this magnitude was taken from (de Grijs 1998, corrected for Galactic extinction, see table 1 in Paper I), and for NGC 5170 from Mathewson & Ford (1996). We have not corrected for internal extinction, because we believe that this could not be reliably performed. For the H I masses of ESO 240-G11 and ESO 435-G25 the single dish values were used due to missing flux at small spacings in the synthesis observations (Section 3.2). For comparison, the Ursa Major cluster sample of Verheijen & Sancisi (2001) is shown (circles), using the *I*-band magnitudes from Tully et al. (1996) and adopting the *Hubble Space Telescope* (*HST*) Key Project distance of 20.7 Mpc (Sakai et al. 2000). A small offset between the two samples appears to be present, although the statistics are poor. Such an offset is expected on the basis of a larger amount of internal extinction due to the high inclinations of our sample galaxies (although several of the Ursa Major cluster spirals are also highly inclined). A rough estimate of the extinction effect can be obtained by comparing the average $I - K$ colours of both samples. The average values for our sample and the Ursa Major sample are 2.3 ± 0.4 (1σ) (de Grijs 1998) and 1.7 ± 0.4 (1σ) magnitudes, respectively. This indicates that the effect of dust extinction is to lower the *I*-band luminosities of our sample (solid dots) by 0.6 *I*-band magnitudes in the case that the extinction in the *K*-band is zero (this lower limit is indicated by the arrow in Fig. 3a).

4.2 H I richness

The H I mass fraction or gas richness, M_{HI}/L_I, has been shown to decrease with increasing luminosity (e.g. Roberts & Haynes 1994;
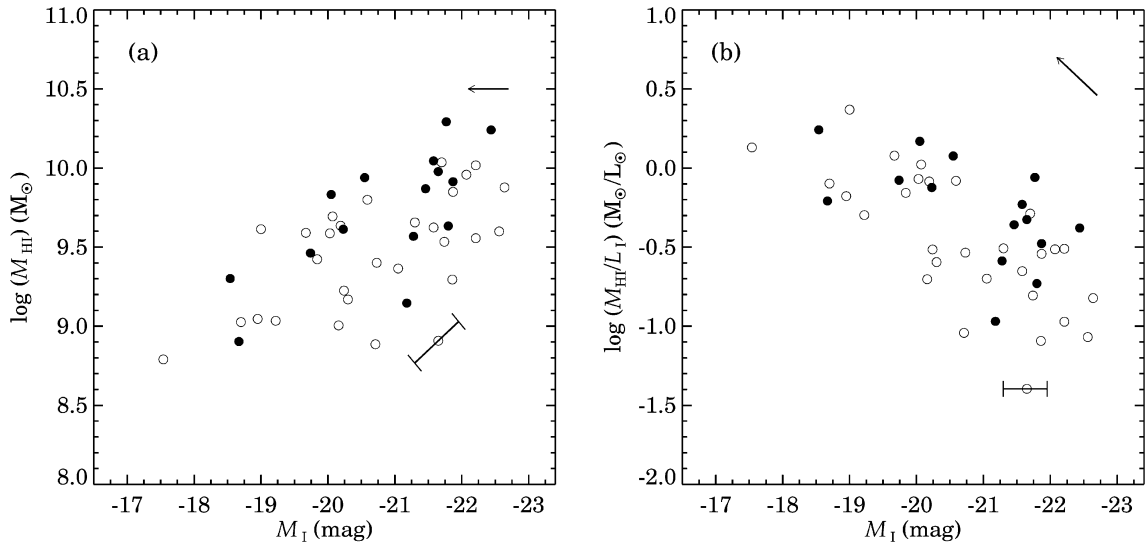
Figure 3. (a) H I mass versus absolute magnitude in *I* band (dots). (b) The H I mass fraction versus absolute magnitude in *I* band (dots). In both panels the sample of Verheijen & Sancisi (2001) is shown for comparison (circles). The arrows indicate an estimate of the effect of extinction (see the text). The bars indicate the effect of a ± 15 per cent distance uncertainty.

Verheijen & Sancisi 2001): spirals of higher luminosity tend to be less rich in H I. Fig. 3(b) shows this relation for our sample, again using the *I*-band luminosity. The relation appears to lie slightly above that found for the Ursa Major cluster (Verheijen & Sancisi 2001). Unlike the small offset in the H I mass luminosity relation, dust extinction is unable to explain this offset. Instead the offset probably indicates that our field spirals tend to be somewhat richer in H I than the spirals of the Ursa Major cluster. The sample average is $M_{H I}/L_I = 0.7 \pm 0.5$ (1σ scatter) $M_\odot/L_\odot$. The H I mass fraction shows no correlation with the stellar disc scalelength or stellar disc flattening.

4.3 The H I mass–size relation

The H I mass–luminosity relation (Section 4.1) is mostly one of size. Previous studies pointed out that the H I mass correlates strongly with both the H I diameter $D_{H I}$ (the diameter at which the H I surface density reaches 1.0 $M_\odot$ pc^{-2}) and the optical diameter D_{25} (measured from the 25.0 *B*-mag arcsec^{-2} isophote). The relation between H I mass and H I diameter for our sample is shown in Fig. 4 (solid dots). It has a logarithmic slope of 1.95 and lies within 0.1 dex of the relations found for samples of less-inclined spirals (e.g. Broeils 1992; Swaters 1999; Verheijen & Sancisi 2001). This good agreement suggests that H I self-absorption cannot have removed more than approximately 20 per cent of the H I flux. The relation between H I mass and the optical diameter D_{25} loses its meaning for highly inclined galaxies. The reason is that the line-of-sight projection causes a higher surface brightness than in the face-on view, depending on the disc flattening, the stellar disc truncation radius R_{max} and the dust distribution. The truncation diameter presents a natural measure of the stellar disc size allowing a more useful comparison with the H I mass. The relation between stellar truncation diameter and the H I mass is also shown in Fig. 4 (open circles), using $2 R_{max}$ for galaxies with a single sided truncation. The relation of H I mass with the stellar truncation diameter is similar to the one with the H I diameter. Or, saying it differently, for the galaxies with detected truncations the radius at which the H I surface density drops to 1.0 $M_\odot$ pc^{-2} is close to the truncation radius, with an average $R_{H I}/R_{max} = 1.1 \pm 0.2$ (1σ). The ratio of H I radius to stellar truncation radius is in agreement with the disc galaxy formation model studied by van den Bosch (2001) for which $R_{H I}/R_{max}$ is close to unity for spirals with
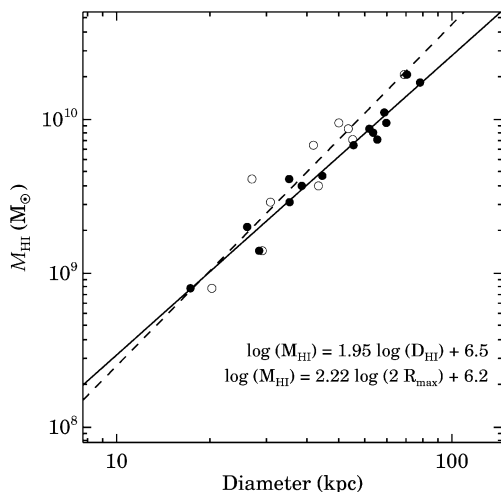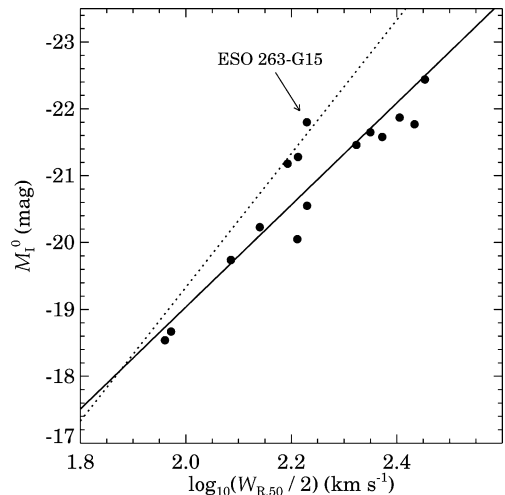
Figure 5. Luminosity–linewidth relation in the *I*-band for 14 edge-on spirals, not corrected for internal extinction (solid dots). The solid line indicates a least-squares bisector fit, and the dotted line indicates the extinction corrected *I*-band luminosity–linewidth relation according to the *HST* Key project (Sakai et al. 2000).

$v_{max} \gtrsim 100$ km s^{-1}. This galaxy formation model is questionable, however, since it does not predict the observed decrease in R_{max}/h_R for stellar discs of a lower face-on central surface brightness (which will be presented in a separate paper, but see Kregel 2003).

4.4 The luminosity–linewidth relation

The offset between the H I mass–luminosity relation for our sample of edge-on spirals and the same relation observed in less inclined spirals (Section 4.1) pointed out that edge-on spirals suffer considerably from dust extinction. A similar offset is expected to show up in the luminosity–linewidth or Tully–Fisher relation (Tully & Fisher 1977). The luminosity–linewidth relation using the *I*-band luminosities (de Grijs 1998) and the linewidths at the 50 per cent level is shown in Fig. 5, rescaled to $H_0 = 71$ km s^{-1} Mpc^{-1} (Sakai et al. 2000). The *I*-band luminosities are uncorrected for internal extinction. The outlier, ESO 263-G15, has a regular H I XV diagram and a well-determined linewidth. Instead its (edge-on) luminosity has probably been overestimated. Given that ESO 263-G15 has a pronounced dust lane (fig. A1 in KKG), it is possible that this overestimate is caused by a serious distance error. A least-squares bisector fit to the entire sample yields a slope $\alpha = 3.05 \pm 0.17$[2] and an intercept $\log_{10}(L_{100}/L_\odot) = 9.27 \pm 0.03$ (solid line). The dotted line indicates the *I*-band luminosity–linewidth relation according to the *HST* Key Project, which has a slope $\alpha = 4.0$ and an intercept $\log_{10}(L_{100}/L_\odot) = 9.39$ (Sakai et al. 2000). This relation uses luminosities that were extinction corrected to the face-on orientation according to the Tully et al. (1998) scheme. The uncorrected *I*-band relation defined by our edge-on systems (solid line) lies systematically below the *HST* Key Project *I*-band relation. Although the sample size is small, the shallower slope of the edge-on relation appears to be robust (a 5σ difference with the *HST* Key Project slope). This implies that the additional extinction in the edge-on orientation steadily increases with linewidth, from values close to zero magnitudes at $W_{R,50}/2 < 80$ km s^{-1} to values on the order of a

Figure 4. H I mass versus the H I diameter (dots) and the stellar disc truncation diameter (circles). The solid and dashed lines show the linear least-squares fits (also indicated in the lower right corner).

---

[2] $L/L_\odot = L_{100}/L_\odot$ [$(W_{R,50}/2)/(100$ km s$^{-1})]^\alpha$, $M_{\odot,I} = 4.14$.

magnitude or more for $W_{R,50}/2 > 200$ km s^{-1}. This effect has also been described and discussed by Giovanelli et al. 1995.

5 SUMMARY

We have presented H I synthesis observations of 15 edge-on spiral galaxies for which the stellar disc structure and kinematics were studied in KKG and Paper I in this series. The main purpose of these observations is the derivation of the H I rotation curves (Paper III) to estimate circular rotation velocities. These will allow us to construct dynamical models of the stellar discs (Paper IV) and constrain the intrinsic stellar disc kinematics and stellar disc mass (Paper V).

We have analysed the global properties, distribution and kinematics of the H I. On the whole, the H I is distributed regularly, showing no strong warps or massive companions. This reflects our selection against spiral galaxies that are optically irregular or strongly warped. The exception is the barred spiral NGC 5529, which is strongly perturbed in both the optical and the H I and has two companions connected to the main galaxy via H I bridges. Several of the spirals are mildly lopsided, but strong lopsidedness, both kinematically and structurally, is present only in ESO 157-G18. For 10 spiral galaxies with a stellar disc truncation we find an average ratio of the H I to truncation radius of $R_{H I}/R_{max} = 1.1 \pm 0.2 \, (1\sigma)$. A comparison of the luminosity–linewidth relation of edge-on spirals with the relation found in less-inclined spirals indicates that the internal extinction increases towards more massive spirals.

REFERENCES

Barnes D.G, et al., 2001, MNRAS, 322, 486
Begeman K.G., 1987, PhD thesis, Univ. Groningen
Bosma A., 1978, PhD thesis, Univ. Groningen
Bottema R., van der Kruit P.C., Freeman K.C., 1987, A&A, 178, 77
Broeils A.H., 1992, PhD thesis, Univ. Groningen
Broeils A.H., Rhee M.-H., 1997, A&A, 324, 877
Davies R.D., Staveley-Smith L., Murray J.D., 1989, MNRAS, 236, 171
de Blok W.J.G., McGaugh S.S., van der Hulst J.M., 1996, MNRAS, 283, 18
de Grijs R., 1997, PhD thesis, Univ. Groningen (http://www.ub.rug.nl/eldoc/dis/science/r.de.grijs)
de Grijs R., 1998, MNRAS, 299, 595
Dickey J.M., Hanson M.M., Helou G., 1990, ApJ, 352, 522
Di Nella H., Paturel G., Walsh A.J., Bottinelli L., Gouguenheim L., Theureau G., 1996, A&AS, 118, 311
García-Ruiz I., Sancisi R., Kuijken K., 2002, A&A, 394, 769
Giovanelli R., Haynes M.P., Salzer J.J., Wegner G., da Costa L.N., Freudling W., 1995, AJ, 110, 1059
Hummel E., 1981, A&A, 93, 93
Kamphuis J., 1993, PhD thesis, Univ. Groningen
Karachentseva V.E., Karachentsev I.D., 2000, Astron. Rep., 44, 501
Kregel M., 2003, PhD thesis, Univ. Groningen (http://www.ub.rug.nl/eldoc/dis/science/m.kregel)
Kregel M., van der Kruit P.C., 2004, MNRAS, submitted (Paper IV)

Table A1. Raw linewidths.

Galaxy	$W_{obs,20}$ (km s^{-1})	$\pm$	$W_{obs,50}$ (km s^{-1})	$\pm$	$W_{lit,20}$ (km s^{-1})	$\pm$	$W_{lit,50}$ (km s^{-1})	$\pm$	R (km s^{-1})	ref.
(1)	(2)	(3)	(4)	(5)	(6)	(7)	(8)	(9)	(10)	(11)
ESO 142-G24	264.5	1.7	249.8	2.4	274	6	260	12	7	a
ESO 157-G18	207.2	1.7	193.7	1.5	213	4	201	4	7	a
ESO 201-G22	357.4	1.1	345.8	1.2	361	4	347	6	7	a
ESO 240-G11	568.8	2.3	549.1	2.9	579	6	555	4	7	a
ESO 263-G15	356.9	3.2	345.6	3.6	356	14	346	10	7	b
ESO 269-G15	352.6	8.0	332.7	7.9	366	8	346	20	7	a
ESO 321-G10	326.0	5.0	318.3	5.0	359	21	326	14	7	c
ESO 416-G25	469.4	4.0	453.9	4.0	441	6	435	4	7	a
ESO 435-G14	292.3	5.1	282.6	3.9	296	12	283	8	10	d
ESO 435-G25	495.8	2.2	477.7	3.1	518	22	480	6	7	a
ESO 435-G50	194.9	3.1	188.8	2.7	198	10	189	6	10	d
ESO 446-G18	434.7	4.0	427.5	4.0	430	27	407	18	10	d
ESO 564-G27	345.9	1.2	331.8	1.6	355	4	338	4	7	a
NGC 5170	526.8	1.1	514.9	1.3	526	10	508	6	7.3	e
NGC 5529	596.8	1.2	590.2	1.3	617	3	575	1	33.5	f

Columns: (1) galaxy; (2) and (3) raw linewidth at the 20 per cent level and error; (4) and (5) raw linewidth at the 50 per cent level and error; (6) and (7) raw linewidth at the 20 per cent level from the literature and error; (8) and (9) raw linewidth at the 50 per cent level from the literature and error; (10) velocity resolution used in the literature measurement; (11) reference, a, Mathewson, Ford & Buchhorn (1992); b, Davies, Staveley-Smith & Murray (1989); c, Di Nella et al. (1996); d, Theureau et al. (1998); e, Staveley-Smith & Davies (1988); f, Rhee & van Albada (1996).

Kregel M., van der Kruit P.C., de Grijs R., 2002, MNRAS, 334, 646 (KKG)

Kregel M., van der Kruit P.C., Freeman K.C., 2004a, MNRAS, in press (Paper I; doi:10.1111/j.1365-2966.2004.07864.x)

Kregel M., van der Kruit P.C., Freeman K.C., 2004b, MNRAS, submitted (Paper V)

Loveday J., 1996, MNRAS, 278, 1025

Lucy L.B., 1974, AJ, 79, 745

Mathewson D.S., Ford V.L., 1996, ApJS, 107, 97

Mathewson D.S., Ford V.L., Buchhorn M., 1992, ApJS, 81, 413

Olling R.P., 1996, AJ, 112, 457

Rhee M.-H., van Albada T.S., 1996, A&AS, 115, 407

Roberts M.S., Haynes M.P., 1994, A&AR, 32, 115

Rupen M.P., 1991, AJ, 102, 48

Sakai S., Mould J.R., Hughes S.M.G., Huchra J.P., 2000, ApJ, 529, 698

Sancisi R., Allen R., 1979, A&A, 74, 73

Sofue Y., 1996, ApJ, 458, 120

Staveley-Smith L., Davies R.D., 1988, MNRAS, 231, 833

Swaters R.A., 1999, PhD thesis, Univ. Groningen (http://www.ub.rug.nl/eldoc/dis/science/r.a.swaters)

Swaters R.A., Sancisi R., van der Hulst J.M., 1997, ApJ, 491, 140

Theureau G., Bottinelli L., Coudreau-Durand N., Gouguenheim L., Hallet N., Loulergue M., Paturel G., Teerikorpi P., 1998, A&AS, 130, 333

Tully R.B., Fisher J.R., 1977, A&A, 54, 661

Tully R.B., Fouqué P., 1985, ApJS, 58, 67

Tully R.B., Verheijen M.A.W., Pierce M.J., Huang J.S., Wainscoat R.J., 1996, AJ, 112, 2471

Tully R.B., Pierce M.J., Huang J.S., Saunders W., Verheijen M.A.W., Witchalls P.L., 1998, AJ, 115, 2264

van den Bosch F.C., 2001, MNRAS, 327, 1334

van der Kruit P.C., Shostak G.S., 1982, A&A, 105, 351

Verheijen M.A.W., Sancisi R., 2001, A&A, 370, 765

Warmels R.H., 1988, A&AS, 72, 427

APPENDIX A: RAW LINEWIDTHS

In Table A1 we list the uncorrected linewidths at the 20 and 50 per cent levels, from both the present synthesis observations and the literature. The linewidths use the optical velocity definition.

This paper has been typeset from a TEX/LATEX file prepared by the author.